

Cryo-EM structure of transmembrane AAA+ protease FtsH in the ADP state

Wu Liu^{1,2,5}, Martien Schoonen^{1,4,5}, Tong Wang³  [✉], Sean McSweeney² & Qun Liu^{1,2}  [✉]

AAA+ proteases regulate numerous physiological and cellular processes through tightly regulated proteolytic cleavage of protein substrates driven by ATP hydrolysis. FtsH is the only known family of membrane-anchored AAA+ proteases essential for membrane protein quality control. Although a spiral staircase rotation mechanism for substrate translocation across the FtsH pore has been proposed, the detailed conformational changes among various states have not been clear due to absence of FtsH structures in these states. We report here the cryo-EM structure for *Thermotoga maritima* FtsH (*Tm*FtsH) in a fully ADP-bound symmetric state. Comparisons of the ADP-state structure with its apo-state and a substrate-engaged yeast YME1 structure show conformational changes in the ATPase domains, rather than the protease domains. A reconstruction of the full-length *Tm*FtsH provides structural insights for the dynamic transmembrane and the periplasmic domains. Our structural analyses expand the understanding of conformational switches between different nucleotide states in ATP hydrolysis by FtsH.

¹Biology Department, Brookhaven National Laboratory, Upton, NY, USA. ²NLSL-II, Brookhaven National Laboratory, Upton, NY, USA. ³Advanced Science Research Center at The Graduate Center, The City University of New York, New York, NY, USA. ⁴Present address: Department of Bioengineering, Lehigh University, Bethlehem, PA, USA. ⁵These authors contributed equally: Wu Liu, Martien Schoonen. ✉email: twang1@gc.cuny.edu; qunliu@bnl.gov

Protein quality control is a major cellular pathway to assure protein homeostasis and their regulated physiological and cellular activities. AAA+ proteases are a family of proteases that proteolytically cleave substrates from which the substrates are unfolded and delivered to the cleavage sites driven by ATP hydrolysis^{1,2}. Among these AAA+ proteases, FtsH (Filamentation Temperature Sensitive Protein H) is the only known family anchored on membranes where it is able to hydrolyze both soluble and membrane protein substrates^{3,4}. The quality control and regulation of membrane proteins by FtsH play a critical role in cell viability and stress resistance in response to changing environments.

FtsH is ubiquitously expressed in prokaryotic and eukaryotic organisms. In bacteria, FtsH proteolytically controls the protein quality of many soluble and membrane proteins⁵. Among these are LpxC in regulating membrane outleaf lipopolysaccharide (LPS) biosynthesis and homeostasis⁶, YfgM in mediating stress response, YccA in regulating membrane protein folding⁷, and transcription factor σ^{32} in heat-shock response⁸. The proteolysis by FtsH is tightly regulated to assure timely and sensitive response of cells to changing environments. For example, the FtsH cleavage of LpxC is further regulated by the recruitment of two additional proteins YciM as a facilitator and YejM as an inhibitor^{9–12}. Eukaryotic FtsHs mainly localize to organelles mitochondria and chloroplasts of prokaryotic origin. In mitochondrial inner membranes, FtsHs have their catalytic domains facing either the cell matrix or interspace, and thus can cleave substrates in either location^{13,14}. In chloroplasts, the well-characterized function of FtsH is to repair the photosystem II (PSII) damage-caused photoinhibition through cleavage of the PS-II reaction center protein D1 subunit^{15,16}. In addition to repairing PSII, in some plants FtsH has lost protease activity while maintaining ATPase activity to drive the import of proteins into chloroplast stroma^{17,18}.

FtsHs contain four domains: N-terminal periplasmic and transmembrane domains and C-terminal ATPase and protease domains. Crystal structures for the ATPase and protease domains suggest that FtsH forms a hexamer with a double-ring structure^{19–21}. The crystal structure of the apo-state *TmFtsH* (FtsH from *Thermotoga maritima*) catalytic domains displays a six-fold symmetry for both the protease and the ATPase domains. Upon ADP binding, the protease domains retain six-fold symmetry, while the six ADP-bound ATPase domains showed a two-

fold or three-fold symmetry in their crystal structures^{20,22,23}. The break of symmetry in the ATPase domains raised a puzzle of how the six-fold apo-state structure changes its conformation to reach the ADP state. It's noted that the ADP-state crystal structure used only the soluble catalytic domains that formed a monomer in solution²⁰. It is possible that under crystallization conditions, intermolecular packing and lattice contacts caused the formation of 2/3-fold symmetry.

There is no crystal structure available for FtsH in an ATP-state; we presume this is due to the significant conformational changes associated with ATP binding and subsequent hydrolysis. Recently, a cryo-EM structure for the catalytic domains of a yeast homolog YME1 provided the first ATP-state structure with a substrate peptide trapped in the ATPase pore²⁴.

Taken as a whole, these FtsH structures indicate the involvement of ATP-binding in substrate translocation through a “spiral staircase” mechanism²⁵. However, these structures do not explain the transition between an ADP-state in resting conditions and an ATP-state during substrate loading and translocation. In addition, except one low-resolution structure²⁶, the FtsH structures available were determined mostly for their catalytic domains, missing the transmembrane and periplasmic domains, raising questions to understand the structure and function of these two domains.

To answer these questions around the relationship of FtsH structure and function, we determined a cryo-EM structure of *TmFtsH* in an ADP-bound state that reveals conformational changes from the ADP-state to apo- and substrate-loaded ATP-states. A reconstruction of the full-length *TmFtsH* suggests dynamic features for the transmembrane and periplasmic domains.

Results

Formation of *TmFtsH*-MSP1D1 nanodiscs. We overexpressed the full-length, protease deficient *TmFtsH* (Fig. 1a) H423Y mutant and purified it in detergents n-Dodecyl-B-D-Maltoside and N,N-Dimethyldodecylamine N-oxide (LDAO) and used negative staining to check particle quality. Neither preparation gave good particles based on electron microscopy analysis using negative staining. Therefore, we expressed a membrane scaffold protein MSP1D1 and reconstituted the purified *TmFtsH* into MSP1D1 nanodiscs in soybean polar lipids. We used

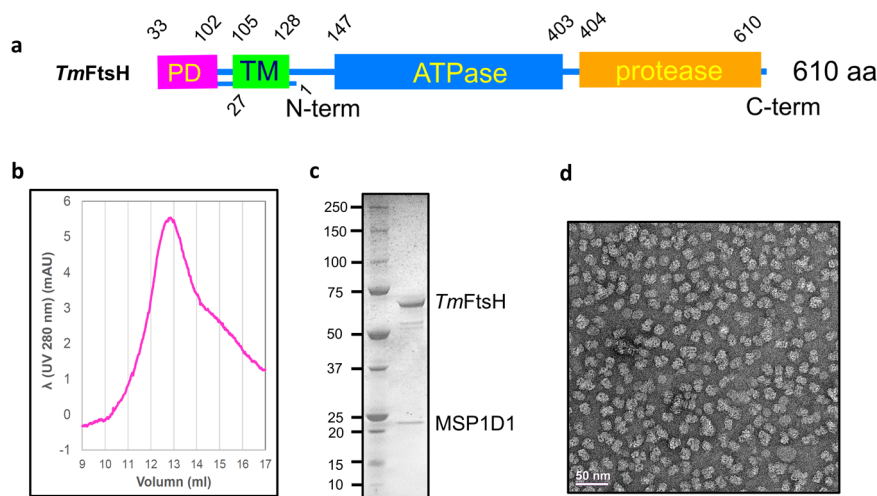


Fig. 1 Production and purification, and characterization of *TmFtsH*. **a** Schematic diagram of *TmFtsH* domains. PD periplasmic domain; TM transmembrane. **b** Size-exclusion chromatography and **c** SDS-PAGE analysis for the purified *TmFtsH* in MSP1D1 nanodiscs. **d** Negative-staining micrograph of *TmFtsH* reconstituted in MSP1D1 nanodiscs.

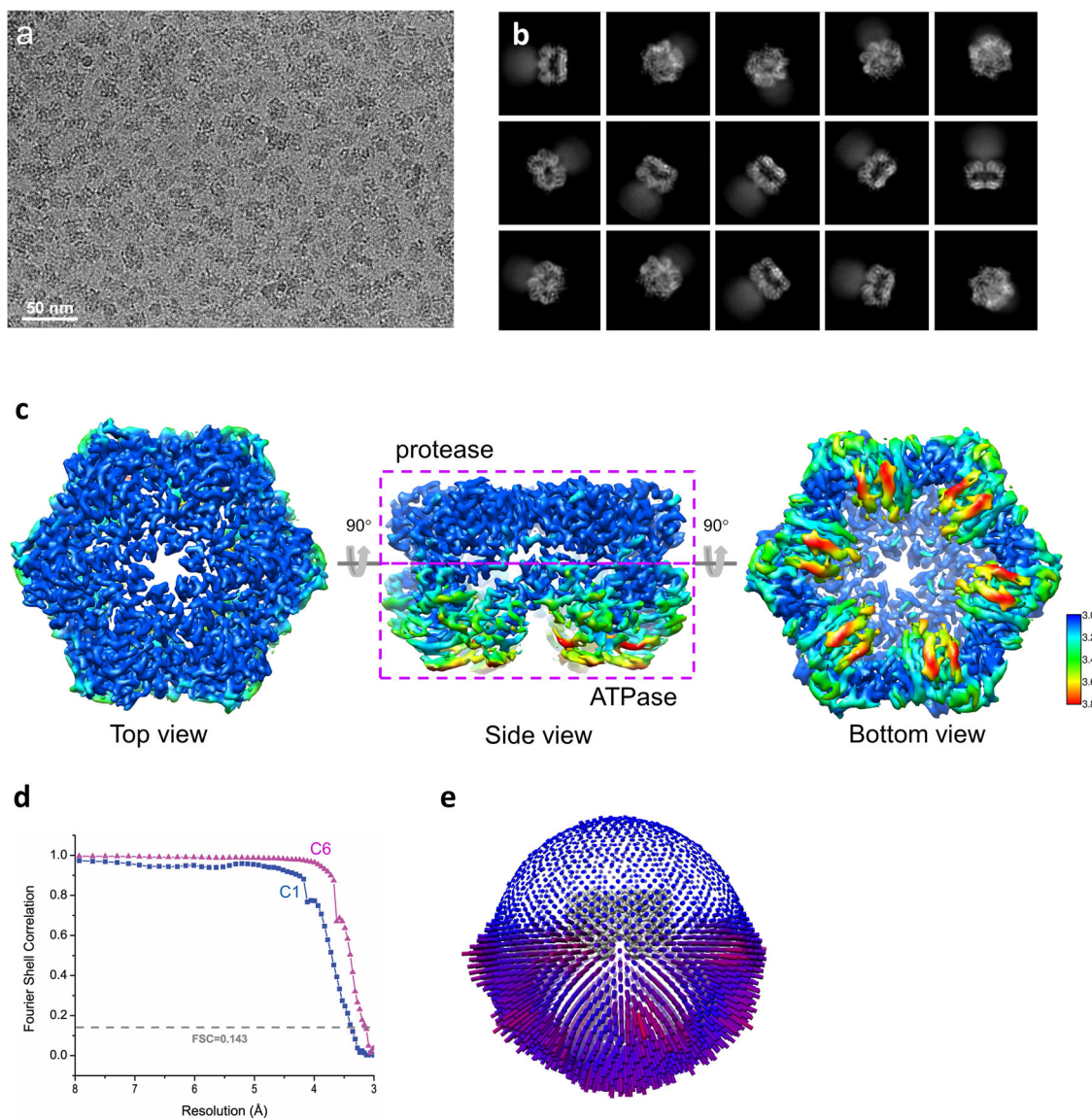


Fig. 2 Determination of *TmFtsH* structure in ADP state. **a** A typical motion-corrected cryo-EM micrograph from a total of 11,169 micrographs. **b** 2D class averages. **c** Three views for the reconstructed map colored with local resolutions. **d** Fourier Shell Correlation (FSC) curve for the 3D reconstruction to determine the structure resolution. **e** Orientation distribution for particles used in the final 3D reconstruction.

size-exclusion column to polish the reconstituted particles and peak fractions containing *TmFtsH* and MSP1D1 (Fig. 1b, c) were pooled together for structural analysis. Figure 1d shows a negative-staining electron micrograph of *TmFtsH* particles in MSP1D1 nanodiscs. These particles display multiple orientations and densities with no apparent aggregates.

Structure determination. For cryo-EM sample preparation, we tested various grids of C-flat, QuantiFoil, and QuantiAuFoil with different hole sizes and blotting conditions. All these preparations resulted in the denaturing of particles during the vitrification process. Only a few particles at the edge of each hole could be picked manually, resulting in an insufficient number of particles for subsequent data analysis. To enrich particles with less denaturation, we used QuantiFoil holey carbon grids coated with 2 nm ultra-thin carbon and added detergent CHAPS (3-cholamidopropyl dimethylammonio 1-propanesulfonate) to the sample prior to vitrification. Such treatment significantly improved the quality of particles, with suitable sizes and distribution, as indicated in Fig. 2a.

We determined the structure of *TmFtsH* following the data analysis workflow as illustrated in Supplementary Fig. 1. 2D class averages show clear structural features for the ATPase and protease domains while with only faint densities for the transmembrane and periplasmic domains (Fig. 2b). Consequently, our final reconstruction at 3.15 Å resolution used 86,652 particles, consisting only the ATPase and protease domains. The reconstructed map used a six-fold symmetry and displays a higher resolution for the protease domains and lower resolution for the ATPase domains (Fig. 2c). As a comparison, a separate reconstruction with no symmetry (C1) yield a lower resolution of 3.4 Å (Fig. 2d). In the final reconstruction, most particles display side views, and fewer particles display views from the bottom (Fig. 2e).

The reconstructed map has a high quality and allows the building and refinement of atomic models. α -helices and β -strands can be clearly seen with characteristic side chains to assist model building and refinement (Supplementary Fig. 2). Although we did not add ADP during the purification and sample preparation steps, we observed densities in the six ATPase

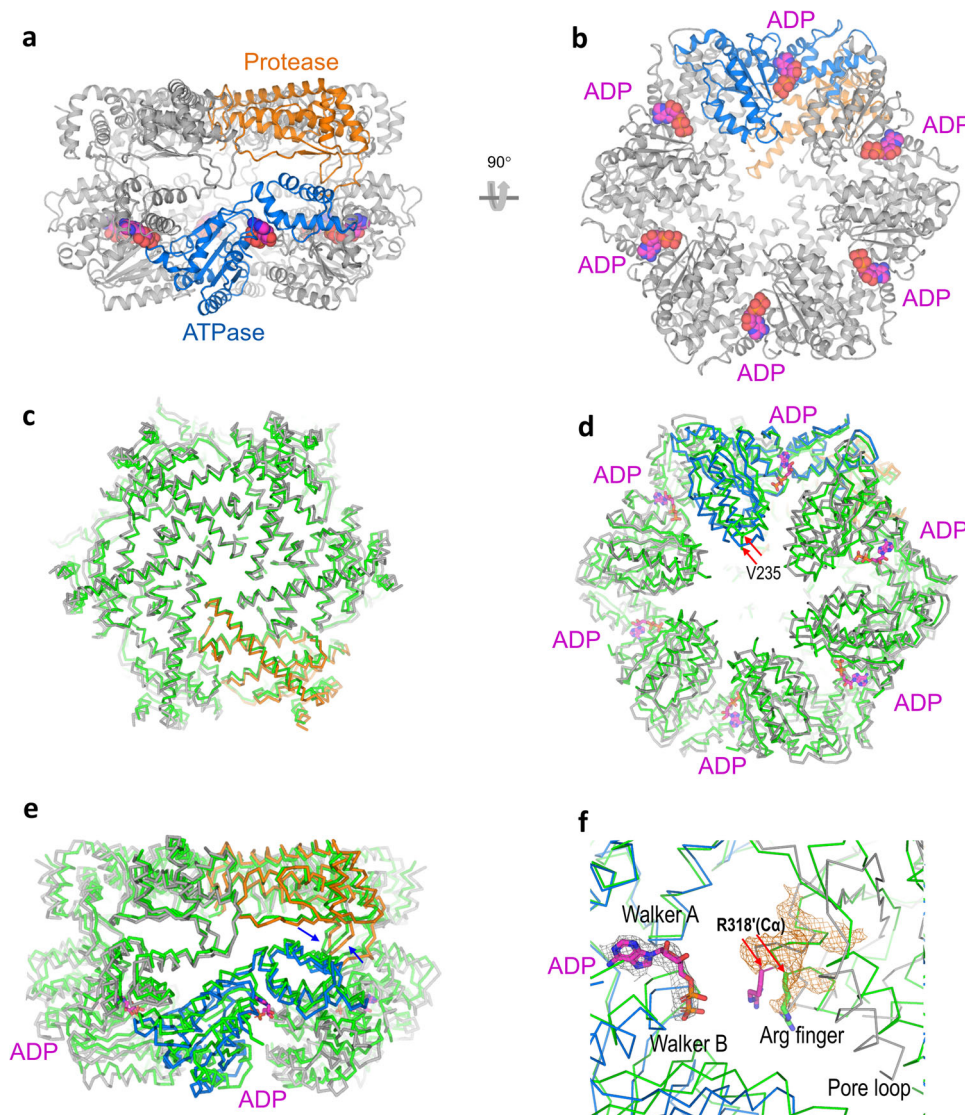


Fig. 3 *TmFtsH* structure in a symmetric ADP state. **a, b** Two views of the overall structure of symmetric protease and ATPases domains. One subunit was colored orange for protease and marine for ATPase, and the rest subunits were colored in gray. ADP molecules are shown as spheres. **c–e** Three views of the superimposition of the ADP-state structure (colored in the same way as in **a** and **b**) with its apo-state crystal structure (PDB code 3KDS, colored in green). Both structures have a six-fold symmetry. The ADP-state structure was colored as in **a**, and the apo-state structure was colored in green. ADP molecules are shown as sticks. Red arrows indicate the Ca atom positions for measuring the distance between two V235 residues. Blue arrows indicate the loops connecting the protease and ATPase domains. **f** Superimposition of ADP-state structure and the apo structure for the binding sites as well as their next clockwise neighboring region. Arginine finger residue R318' is shown as magenta (ADP-state) and green (apo-state). Red arrows indicated the Ca atom positions for measuring distance. Cryo-EM densities for ADP and the R318' regions were colored as gray and orange isomeshes, respectively.

domains when we refined the map with or without symmetry (Supplementary Fig. 3). ADP bound endogenously to *TmFtsH* and survived the co-purification and reconstitution processes. Our cryo-EM structure may thus represent a fully ADP-bound resting state structure in a six-fold symmetry under physiological conditions. As we used a zinc-binding-deficient mutant H423Y for cryo-EM analysis, we did not model zinc ions in the protease domains. Our refined model consists of 2484 residues and six ADP molecules (Fig. 3a, b).

Apo-ADP state transition. The apo-state *TmFtsH* crystal structure for its catalytic domains has been previously determined with a six-fold symmetry¹⁹. We thus compared the apo- and ADP-state structures for seeking conformational changes induced by ADP binding. We attempted to align both structures based on overall, protease domains, and ATPase domains. We found that

the best alignment was based on the protease domains (residues 404–603) with an RMSD of 2.0 Å for 1128 aligned Ca atoms (Fig. 3c). With the alignment, the side view of the two hexamers indicated conformational changes in the ATPase domains starting from the linker loops to their protease domains (Fig. 3d, e and Supplementary Fig. 4a). Consequently, the bottom view indicated a shrink of the ATPase pore from the apo to ADP state by a movement of 4.5 Å as measured by the distance between the Ca atoms of residue V235 which is located on the tip of a pore loop (Fig. 3d).

Compared with the apo-state structure, ADP-binding triggered larger conformational changes for the Walker B region structure than the Walker A region structure (Fig. 3f). In addition, there are structural changes for the arginine finger in the next clockwise subunit where residue R318' Ca atom ("R318'" denotes next clockwise subunit) moved 3.6 Å closer to the ADP phosphate

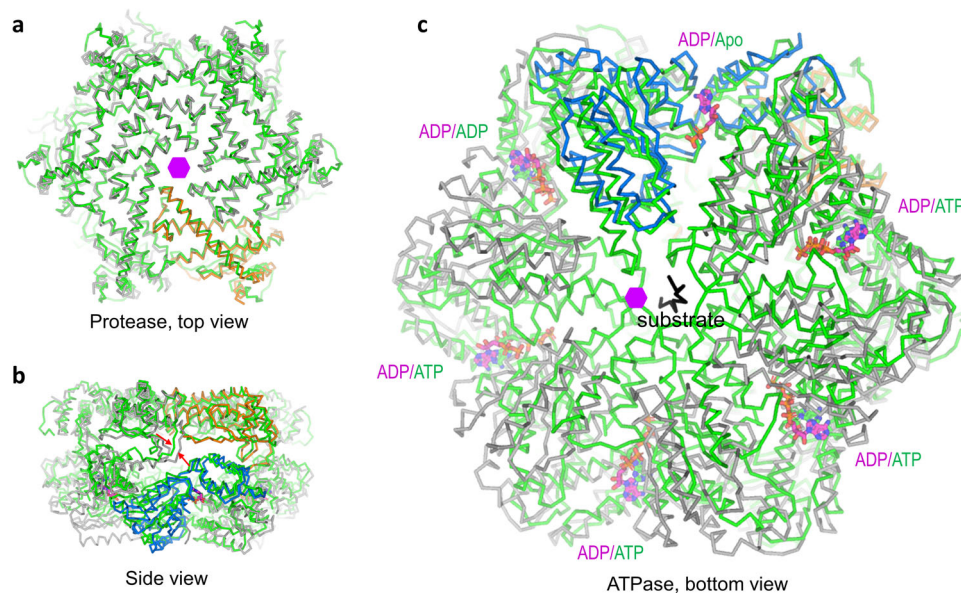


Fig. 4 Structural comparison of ADP-state structure with a substrate loaded yeast homolog structure YME1. **a** Top view to show the alignment for the protease domain. YME1 structure (PDB code 6AZO) is colored in green; ADP-state *TmFtsH* structure is colored in orange and gray. **b** Side view to show both protease and ATPase domains. Red arrows indicate the loops connecting the protease and ATPase domains. **c** Bottom view to show the alignment for the ATPase domains. ADP and ATP molecules are shown as sticks (magenta for *TmFtsH* and green for YME1). Substrate is colored in black. Colors of the rest structures are the same as those of Fig. 3c–e. A magenta hexagon indicates the center of the symmetric ADP-state hexamer.

groups in the ADP-state structure (Fig. 3f). We observed that conformational changes in the arginine finger propagates to a disordered loop which is involved in substrate engagement and translocation (see below). However, we did not observe side chain densities for R318'. So, we used its mainchain C α position and a sidechain rotamer to depict the residue position to illustrate structural changes. We propose that the R318' sidechain amide groups may interact weakly with these negatively charged ADP phosphate groups, thus promoting a movement of the arginine finger closer to the ADP phosphate groups upon ADP binding. The apo-state structure is symmetric; ATP-binding and hydrolysis-induced conformational changes in the next clockwise subunit propagate throughout the hexamer. When all six ADP molecules bound in the hexamer, a new symmetric state, i.e. the ADP-state, is reached.

ADP-ATP state transition. To further understand the detailed conformational changes from ADP to ATP state prior to ATP-hydrolysis, we aligned *TmFtsH* with a yeast homolog structure YME1 bound with four ATP molecules and a substrate peptide²⁴. *TmFtsH* and YME1 share a sequence identity of 37.2% (227 out of 610 residues). Similar to the alignment with the apo structure, *TmFtsH* aligned well with the YME1 structure for the protease domains with an RMSD of 2.6 Å for 846 aligned C α atoms (Fig. 4a). Conformational changes among the two structures are in the ATPase domains starting from the loops connecting their protease domains and are best viewed from the side of the two domains (Fig. 4b and Supplementary Fig. 4b). Compared with the protease domains, drastic conformational changes are seen in the ATPase domains (Fig. 4c). The YME1 hexamer contains four ATP, one ADP, and one empty site, thus providing a good reference to see conformational changes from the ADP- to ATP-state transition. Overall, ATP and ADP molecules in both structures overlap well. Upon ATP binding, its clockwise neighboring subunit changes its conformation, causing asymmetrical shrinkage of the pore relative to the center in the symmetric six-fold ADP-state structure (Fig. 4c).

Based on our structural analysis of the ADP-state with the apo *TmFtsH* and substrate-loaded YME1 structures, it seems clear that ATP-binding and perhaps also substrate loading are required to break the six-fold symmetry. In absence of ATP, the conformational changes induced by ADP binding appear not big enough to create a tight pore for substrate engagement (Fig. 3d). We obtained the ADP-state structure without adding ADP or ATP during protein purification and cryo-EM sample preparation. This suggests that our ADP-state structure provides a basis to understand ATP-binding-dependent conformational changes.

Comparison with the ADP-bound crystal structure. The ADP-bound crystal structure of the *TmFtsH* intracellular domains shows a mixed symmetry: six-fold for the protease domains and two-fold for the ATPase domains²³. However, in our ADP-bound cryo-EM structure, we have both protease and ATPase domains in the six-fold symmetry. On the hexamer level, the two structures can only be aligned on the protease domains with an RMSD of 3.4 Å for 1010 aligned C α atoms (Fig. 5a). In contrast, there are substantial conformational changes observed for the ATPase domains, and ADP molecules belonging to the same subunit did not align well (Fig. 5b). In the ADP-bound cryo-EM structure, the six ADP molecules are close to R318' from their next clockwise neighboring subunits (Fig. 3f). As a comparison, in the ADP-bound crystal structure, four ADP molecules are close to their neighboring R318'; while the remaining two ADP molecules are further away from their neighboring R318', suggesting very weak or no interactions (Fig. 5c).

In order to see detailed conformational changes between the two ADP-bound structures, we aligned one subunit of the cryo-EM structure with each of the three non-symmetric subunits in the crystal structure (Fig. 5d–f). With the alignments against the protease domain, conformational changes are in the ATPase domains starting on the loops (residues 403–410) connecting to the protease domain. These loops were ordered in the cryo-EM structure but disordered in the crystal structure for all subunits. In addition, in two of the three subunits, an 18-amino-acid loop

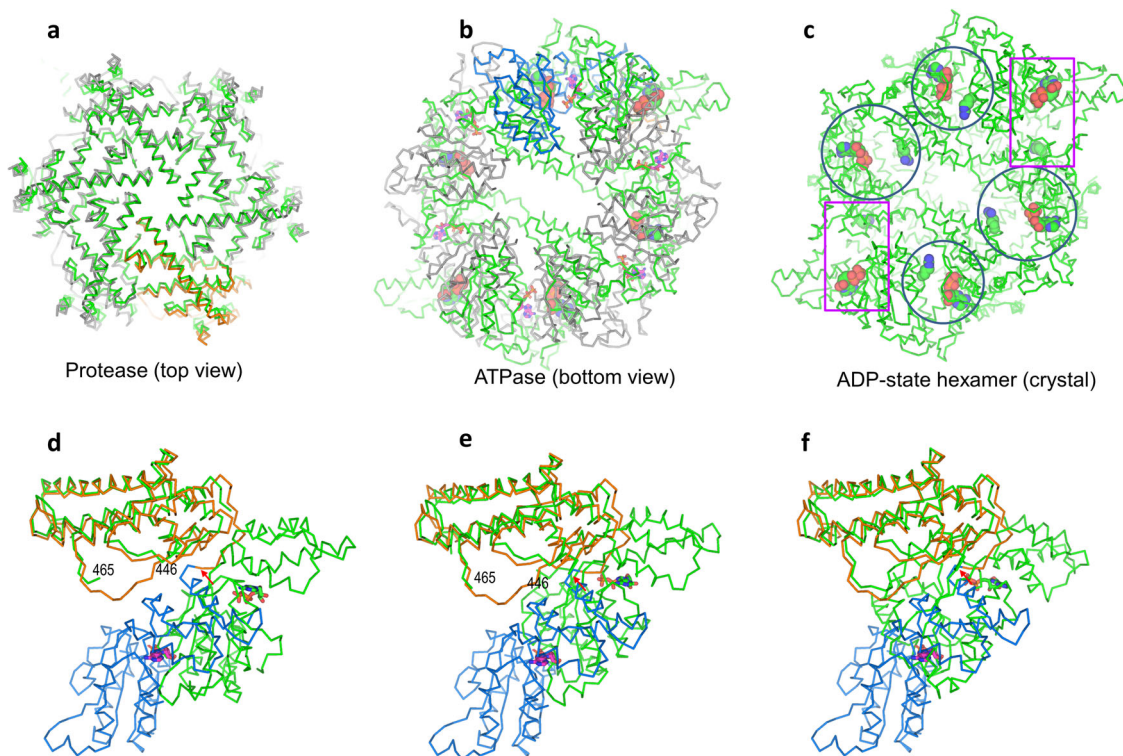


Fig. 5 Structural comparison of ADP-state cryo-EM and crystal structures. The crystal structure used for comparison is *TmFtsH* intracellular domains (ATPase and protease) crystallized in a mixed C2/C6 symmetry (PDB code 2CEA). Two views to show the alignments for the protease (**a**) and ATPase (**b**) domains. ADP molecules are shown as sticks in cryo-EM structure and spheres in the crystal structure. Colors of the two structures are the same as in Fig. 3c–e. **c** Bottom view of the ADP-bound crystal structure for the ATPase domains to show the relative separation of ADP (orange spheres for carbon) and arginine finger residue R381 (green spheres for carbon). Circles and rectangular boxes indicate nearby and far away ADP-R381 pairs, respectively. **d–f** Side-view comparisons of one ADP-state subunit with three non-symmetric equivalents in the crystal structure. ADP molecules are shown as sticks: magenta for cryo-EM structure and green for crystal structure. Red arrows indicate the loops (disordered in the crystal structure) between the protease and ATPase domains.

in the protease domain (residues 447–464) is also disordered while the equivalent loops are ordered in the cryo-EM structure (Fig. 5d, e).

The ADP-bound crystal structure used only the catalytic domains (protease and ATPase) that formed a monomer in solution²⁰ whereas, our cryo-EM structure used the full-length protein. It is possible that under crystallization conditions, intermolecular packing and lattice contacts caused the formation of a distorted hexameric structure. We therefore argue that *TmFtsH* in its fully bound ADP state should be interpreted as a six-fold symmetric structure for both the protease and ATPase domains.

Full-length structure. During our classification of the intracellular *TmFtsH* hexamer, we found 2D classes that showed blurred transmembrane and periplasmic domains (Fig. 2b). We attributed this blurring to the denaturation of the two domains during the vitrification process. To obtain the full-length *TmFtsH* reconstruction, we selected 2D classes generously and did extensive 2D classifications to find those rare 2D classes with best images for the transmembrane and periplasmic domains as shown in Fig. 6a. Through this 2D classification process, we were able to select 7468 particles, which mainly are side views. We excluded all top-view particles as it's difficult to see from projected views for the existence of transmembrane and periplasmic domains.

We then did *ab initio* 3D reconstruction, heterogeneous, and homogenous refinements in CryoSPARC and obtained a reconstruction map at an overall resolution of 7.9 Å without symmetry (Fig. 6b, c). The local resolution map shows that the

intracellular domains have a higher resolution relative to the transmembrane and periplasmic domains (Fig. 6b). For the transmembrane domain, we could not detect α -helical features likely due to the disordering of the domain. Nevertheless, there are connecting densities between the transmembrane and periplasmic domains (Fig. 6b).

To produce a model to interpret the poorly defined transmembrane and periplasmic domains, we used AlphaFold²⁷ to assemble a hexameric model consisting of residues 1–134 and fitted the model into the density using Chimera (Fig. 6d, e). Relative to the intracellular protease and ATPase domains, the transmembrane and periplasmic domains tilted at the membrane surface by about 20°. Structurally, this tilted structure could be of biological relevance in allowing the proximity of substrates to the ATPase pore loops, thus promoting substrate recognition. Similar tilting has been suggested to be beneficial for the recognition and loading of membrane protein substrates²⁸.

Discussion

There have been crystal structures for the soluble catalytic domains of the ADP-state structures for *TmFtsH* and its bacterial homologs^{20,22,29}. These structures were determined in a six-fold symmetry for the protease domains and two- or three-fold symmetry for the ATPase domains with fully loaded ADP molecules. Comparison of our ADP-bound cryo-EM structure with its crystal structure suggests that *TmFtsH* ADP-state structure should be symmetric for both protease and ATPase domains (Fig. 5). Symmetric ADP-state cryo-EM structure provides a consistent picture to explain the conformational changes from

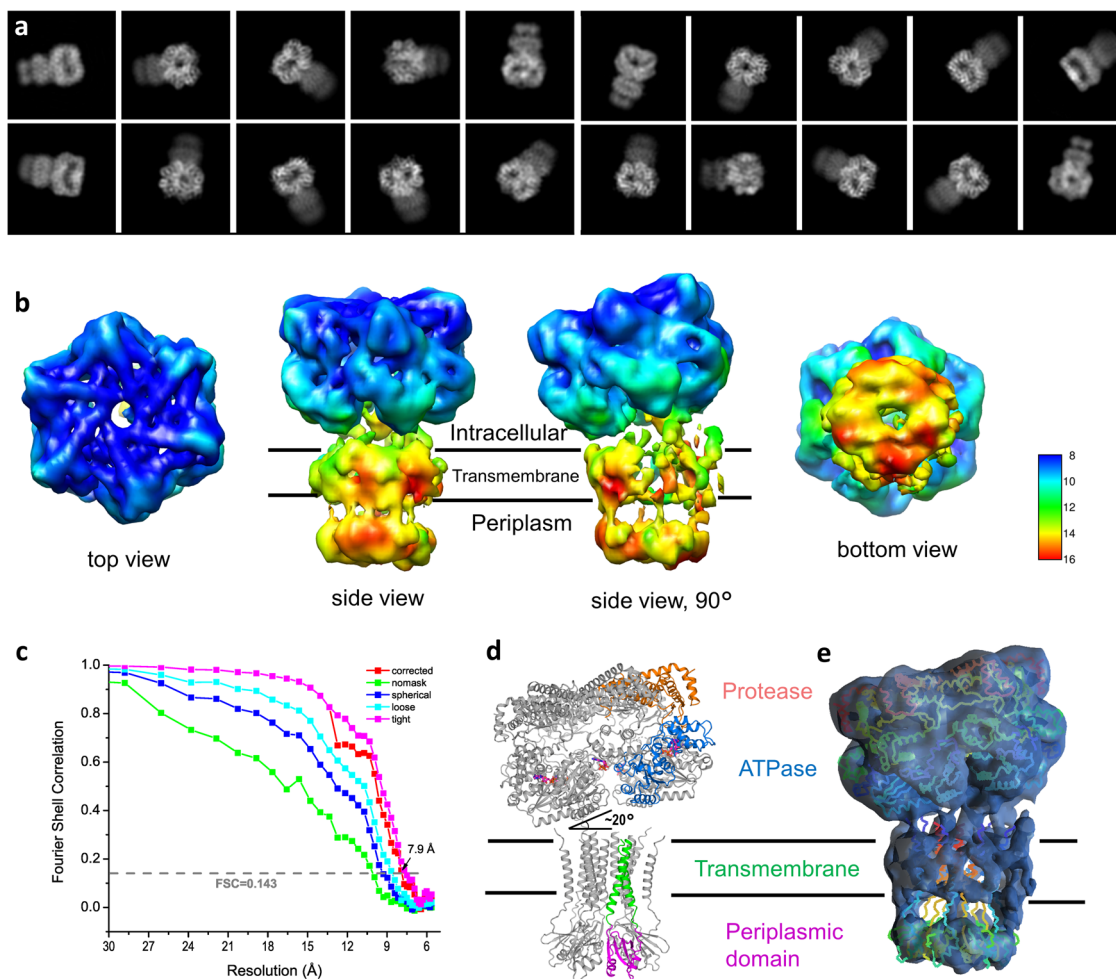


Fig. 6 Full-length *TmFtsH* reconstruction at a low resolution. **a** Selected views of 2D class averages showing full-length *TmFtsH*. **b** Four views of the reconstructed 3D map colored with local resolutions. **c** Gold-standard Fourier Shell Correlation. **d** A full-length *TmFtsH* model with the transmembrane and periplasmic domains built by AlphaFold. **e** Fitting of the full-length *TmFtsH* model into the density map.

apo to ADP-state through direct ADP-binding or ATP-hydrolysis induced movement of neighboring ATPase domains (Fig. 4d).

ATP-binding breaks the symmetry as shown in the YME1 structure²⁴. We attempted to observe the breakage of *TmFtsH* symmetry by ATP binding using cryo-EM. We added 5–10 mM ATP and 5 mM Mg²⁺ to the protein and waited for 5–10 min before vitrification. We collected and processed cryo-EM data as we did for the ADP-state. However, the reconstructed structure remained in a symmetric ADP-state with six ADP molecules in the ATPase domains. It's possible that our protease deficient H423Y mutant³⁰ was active and hydrolyzed ATP to ADP. Using an ATP analog or a *TmFtsH* mutant in the ATPase Walter B site might be possible solutions to obtain the *TmFtsH* structure in its ATP state³¹.

FtsHs have been proposed to form complexes with quite a few membrane protein substrates such as YccA³², YfgM³³, YciM¹¹, and YqgP³⁴. To get a high-resolution reconstruction for the transmembrane regions, one perhaps needs to have a well-formed complex between FtsH and its membrane protein substrate. Since ATP is needed for substrate engagement and translocation, the complex formation may also need ATP and a mutation in the ATP-binding site to slow down the ATP hydrolysis. This combined strategy will likely allow one to capture a high-resolution structure for the transmembrane and periplasmic domains in complex with a membrane protein substrate.

With the recently released AlphaFold algorithm for protein structure prediction, we were able to produce a hexameric model for the transmembrane and periplasmic domains to understand the low-resolution cryo-EM map for the full-length *TmFtsH*. The model contains 12 transmembrane helices with loops connecting to periplasmic domains that form an oligomer in its crystal structure³⁵. The predicted periplasmic domain structure is almost identical to its crystal structure with an RMSD of 1.3 Å for 200 aligned Ca atoms. However, the predicted transmembrane helices and their relative orientation to the periplasmic domains need to be further validated by a high-resolution structure.

The most well-studied function of FtsH is to cleave substrate proteins through which to control protein quality and homeostasis. As suggested by the full-length cryo-EM map, transmembrane and periplasmic domains are quite flexible compared to intracellular domains. Such a flexibility may be essential for their interactions with other proteins to acquire additional functions other than the protease function. One example is FtsH-inactive (FtsHi) proteins in plant chloroplasts where they form a large complex to import proteins into chloroplasts¹⁷. This function does not require the protease activity. It is thus possible that FtsH may form a translocation complex in which ATPase domains recognize and unfold substrate protein and deliver the unfolded protein for importing across the inner chloroplast membranes. In addition to FtsH, there are AAA+ protein

translocators that can indeed transport proteins across mitochondrial inner membranes^{36,37}.

With the ADP-state structure and its structural comparisons with the apo and substrate-loaded states, we could propose a process for the initial substrate loading and conformational changes. Under the resting conditions, FtsH is a symmetric hexamer, fully loaded with ADP in its six subunits. The intracellular protease and ATPase domains dynamically float over the membrane surface through the loops between the ATPase and transmembrane domains. A nearby substrate interacts to and is recognized by the ATPase pore loops. Such interactions are facilitated by tilting and the disordered loops between the ATPase and transmembrane proteins. For membrane protein substrates, hydrophobic interactions between their transmembrane domains may help to bring substrate close to the ATPase pore for facilitated substrate recognition and loading. When ATP is available, its binding triggers conformational changes of its clockwise next neighboring subunit which will break the six-fold symmetry and induce conformational changes to engage substrate. Subsequent ATP hydrolysis and translocation will follow the proposed spiral staircase mechanism²⁵ to pull the substrate through the ATPase pore and deliver it to the protease site for proteolytic cleavage.

Methods

Protein expression and purification. The cDNA sequence encoding the full length of FtsH of *Thermotoga maritima* (*TmFtsH*) was cloned into pET24-derived pMSCG-7 plasmid³⁸. Using this plasmid as a template, FtsH H423Y mutation was generated by one-step site-directed mutagenesis³⁹. After verification of the mutation by DNA sequencing, it was expressed in *Escherichia coli* BL21 (DE3) pLysS cells growing in Terrific Broth medium. After induction by 0.2 mM Isopropyl β -D-1-Thiogalactopyranoside (IPTG) at 16 °C for 18 h, the cells were harvested by centrifugation at 5000 rpm for 10 min using a Sorvall SLC-4000 rotor. Cell pellets were resuspended in lysis buffer (40 mM Tris, pH 8.0, 250 mM NaCl, 10% glycerol) supplemented by 1 mM phenylmethanesulfonyl fluoride (PMSF, 100 mM stock in alcohol). Cells were lysed using an EmulsiFlex-C3 homogenizer (Avestin, Ottawa, Canada) at 10,000–15,000 psi for four passages. After another centrifugation at 16,000 rpm for 30 min using a Ti45 rotor, supernatant was collected, and the membrane was obtained by ultra-centrifugation at 36,000 rpm for 60 min using the Ti45 rotor.

Cell membranes were resuspended in solubilization buffer (40 mM Tris, pH 8.0, 250 mM NaCl, 10% glycerol, 0.5 mM TCEP, 1 mM AEBSE, 10 mM imidazole, 1.5% w/v LDAO, and Roche protease inhibitor cocktail) and stirred using a magnetic mixer. After 1 h, the solubilization mixture was ultra-centrifuged (Ti45 Rotor, 36,000 rpm) for 30 mins to remove the insoluble part. The supernatant was then passed through a pre-equilibrated HisTrap HP column (GE Healthcare, Chicago, USA) twice. The column was washed using a step gradient concentration of wash buffer (40 mM Tris, pH 8.0, 250 mM NaCl, 10% glycerol, 0.5 mM TCEP, 1 mM AEBSE, 0.06% w/v LDAO) supplemented with imidazole of 10, 50, 75, and 100 mM. The target protein was eluted using elution buffer (40 mM Tris, pH 8.0, 250 mM NaCl, 10% glycerol, 0.5 mM TCEP, 1 mM AEBSE, 0.06% w/v LDAO, and 300 mM imidazole). The eluted protein was polished by gel filtration on a Superose 6 10/300 increase column (GE Healthcare, Chicago, USA) with elution buffer of 20 mM HEPES, pH 7.6, 500 mM NaCl, 5% glycerol, 0.5 mM TCEP, and 0.06% w/v LDAO. Fractions containing the protein were pulled together and concentrated to ~1 mg/ml. Through the *TmFtsH* solubilization and purification processes, ADP or ATP-Mg²⁺ was not used in the buffer.

MSP1D1 and lipids preparation. Membrane scaffold protein MSP1D1 was expressed and purified from *E. coli* BL21 (DE3) pLysS cells⁴⁰. Soybean polar lipids extracts (Avanti Polar Lipids, Inc., Birmingham, USA) were dissolved in chloroform and were transferred to glass tubes, dried under a nitrogen stream for 3 h. Residual chloroform was further removed by vacuum desiccation at 15 psi overnight, and the dried lipid films were resuspended in a buffer (100 mM sodium cholate, 20 mM HEPES, pH 7.6, 500 mM NaCl, 2 mM TCEP, 0.5 mM EDTA) and solicited for 1 hr in a bath sonicator until the liquid became clear. Finally, 50 mM soybean polar lipids were prepared in buffer containing 100 mM sodium cholate, 20 mM HEPES, pH 7.6, 500 mM NaCl, 2 mM TCEP, and 0.5 mM EDTA.

***TmFtsH*-MSP nanodisc formation.** Reconstitution of *TmFtsH*-MSP nanodiscs was based on the published method⁴⁰. Briefly, purified protein in buffer A (20 mM HEPES, pH 7.6, 0.5 mM TCEP, 0.06% w/v LDAO) was mixed with buffer B (100 mM sodium cholate, 20 mM HEPES, pH 7.6, 500 mM NaCl, 2 mM TCEP, 0.5 mM EDTA) to make a final concentration of sodium cholate at 25 mM. Then, soybean polar lipids and MSP1D1 were added to reach a final lipid concentration

of 0.32 mM and MSP1D1 concentration of 3.2 μ M. The molar ratio of hexameric *TmFtsH*:MSP1D1:lipid was 1:4:100. This mixture was incubated on ice for 1 h. Bio-beads SM2 (4 mg, Bio-Rad, Hercules, USA) were then added to the mixture, and the mixture was incubated at 4 °C for 1 h with constant rotation. A second batch of Bio-beads (8 mg) was added, and the mixture was incubated at 4 °C for 9 h with constant rotation. The reconstitution mixture was centrifuged and the supernatant was used for gel filtration through a Superose 6 increase column (GE Healthcare) in a buffer containing 20 mM HEPES, pH 7.6, 150 mM NaCl, and 0.5 mM TCEP. The fractions containing the *TmFtsH*-MSP nanodiscs were collected, concentrated to about 1 mg/ml, and flash frozen for storage at -80 °C. ADP or ATP-Mg²⁺ was not used in the buffer for FtsH-MSP nanodisc formation.

Negative stained sample preparation. Glow-discharged continuous carbon grids (Cat# CF300-CU-UL, Electron Microscopy Sciences, Hatfield, PA) were used for negative staining. The sample was diluted 10 \times in the elution buffer (20 mM HEPES, pH 7.6, 150 mM NaCl, and 0.5 mM TCEP) and 3 μ l was applied on the carbon side of the grid. After incubation for 1 min, extra protein was washed away by touching a piece of filter paper followed by two washes in 10 μ l distilled water and one wash in 2% uranium acetate (UA). The sample was then stained using 2% UA for 1 min and excess liquid was wicked out using a filter paper. The stained sample was dried in air and evaluated on a JEOL-1400 Electron Microscope (JEOL USA inc, Peabody, USA).

Cryo-EM sample preparation and data collection. *TmFtsH*-MSP1D1 nanodiscs were diluted by four times in a buffer containing 20 mM HEPES, pH 7.6, and 100 mM NaCl. The diluted sample was mixed briefly with CHAPS (3-((3-cholamidopropyl) dimethylammonio)-1-propanesulfonate) to a final CHAPS concentration of 0.05% (w/v). Three microliters of the mixed sample were immediately applied to a glow-discharged (15 mA current for 15 s) 300-mesh QUANTIFOIL R1.2/1.3 2 nm ultra-thin carbon grid (Cat# Q350CR1.3–2 nm, Electron Microscopy Sciences, Hatfield, PA). After waiting for 60 s, vitrification was performed using a

Table 1 Cryo-EM data collection, 3D reconstruction, and refinement statistics.

| Data collection | |
|---|-------------------------------|
| Microscope | Titan Krios G3i |
| Stage type | Autoloader |
| Voltage (kV) | 300 |
| Detector | Gatan K3 |
| Energy filter (eV) | 20 |
| Acquisition mode | Super-resolution |
| Physical pixel size (Å) | 0.684 |
| Defocus range (μ m) | 0.7–2.5 |
| Electron exposure (e ⁻ /Å ²) | 61 |
| Reconstruction | |
| Software | Relion v3.08, CryoSPARC v2.15 |
| Particles picked | 2,548,908 |
| Particles final | 86,652 |
| Extraction box size (pixels) | 400 |
| Rescaled box size (pixels) | 64 |
| Final pixel size | 1.368 |
| Map resolution (Å) | 3.15 |
| Map sharpening B-factor (Å ²) | 100 |
| Model refinement | |
| Software | PHENIX |
| Refinement algorithm | Real Space |
| Clipped box size (pixels) | None |
| Number of residues | 2484 |
| Number of ADP | 6 |
| R.m.s deviations | |
| Bond length (Å) | 0.003 |
| Bond angle (°) | 0.542 |
| Molprobrity clashscore | 4.71 |
| Rotamer outliers (%) | 0.0 |
| C β deviations (%) | 0.0 |
| Ramachandran plot | |
| Favored (%) | 95.89 |
| Allowed (%) | 4.11 |
| Outliers (%) | 0 |
| PDB code | 7TDO |

ThermoFisher Mark IV vitrobot with a blotting condition of 3.5 s blot time, 0 blot force, and 100% humidity at 6 °C.

Cryo-EM data were collected with the use of a ThermoFisher Titan Krios (G3i) equipped with a Gatan K3 camera and a BioQuantum energy filter. With a physical pixel size of 0.684 Å, a total dose of 61 e⁻/Å² were fractioned to 51 frames under the super-resolution mode using the ThermoFisher data acquisition program EPU. A total of 11,169 movies were collected with an energy filter width of 20 eV throughout the data acquisition. Data collection statistics are listed in Table 1.

Cryo-EM data processing. Beam-induced motion correction was performed using MotionCorr²⁴¹ with a bin-factor of 2. Corrected and averaged micrographs were further corrected by CTF estimation using Gctf⁴². Micrographs with an estimated resolution better than 4.5 Å were selected for further processing. Particle picking and extraction were performed using Localpicker⁴³ and Relion3⁴⁴. A total of 2,548,908 particles were picked, extracted at 400 pixels, and binned to 64 pixels with a pixel size of 4.49 Å.

We used CryoSPARC⁴⁵ and Relion3 for 2D and 3D class averages and 3D refinements. Specifically, we used 2D class averaging for initial particle cleanup which resulted in 842,697 particles. Using these particles, we produced an initial 3D map in CryoSPARC and used it to perform 3D homogenous refinements (Supplementary Fig. 1). Then these particles were selected, re-centered, re-extracted at 400 pixels, and binned to 200 pixels with a pixel size of 1.368 Å.

Extracted particles were auto refined to convergence in Relion3 followed by non-alignment 3D classification into five classes (Supplementary Fig. 1). Particles from the 3D class with the best structural feature as visualized in Chimera⁴⁶ were selected. Particles from the best class (15.4%) were selected for CTF refinement and Bayesian polishing in Relion3, and 2D classification and non-uniform refinement in CryoSPARC to reach a refined reconstruction based on gold-standard Fourier Shell Correlation of 0.143 (Fig. 2d). The final reconstruction used 86,652 particles. Local resolutions were estimated using BlocRes⁴⁷. Reconstruction statistics are listed in Table 1.

Model building and refinement. To assist our model building and refinement, we sharpened the masked and filtered map using PHENIX⁴⁸ with a B factor of -100 Å². We used the PDB code 3KDS as a starting model and built the model for TmFtsH and ADP in COOT⁴⁹ and refined the model iteratively in PHENIX. The refined model was validated using Molprobity⁵⁰ and the refinement statistics are listed in Table 1. The model for the hexameric transmembrane and periplasmic domains were built using ColabFold⁵¹, a modified version of AlphaFold²⁷, and was fitted into the cryo-EM map as a rigid body in Chimera.

Reporting summary. Further information on research design is available in the Nature Research Reporting Summary linked to this article.

Data availability

The three-dimensional cryo-EM density map has been deposited in the Electron Microscopy Data Bank under the accession number EMD-25837. Atomic coordinates have been deposited in the Protein Data Bank under the accession number 7TDO. Source data for Fig. 1c are available in Supplementary Data 1.

Received: 19 November 2021; Accepted: 1 March 2022;

Published online: 23 March 2022

References

- Sauer, R. T. & Baker, T. A. AAA+ proteases: ATP-fueled machines of protein destruction. *Annu. Rev. Biochem.* **80**, 587–612 (2011).
- Zhang, S. & Mao, Y. AAA+ ATPases in protein degradation: Structures, functions, and mechanisms. *Biomolecules* **10**, 629 (2020).
- Langklotz, S., Baumann, U. & Narberhaus, F. Structure and function of the bacterial AA protease FtsH. *Biochim. Biophys. Acta Mol. Cell Res.* **1823**, 40–48 (2012).
- Janska, H., Kwasniak, M. & Szczepanowska, J. Protein quality control in organelles—AAA/FtsH story. *Biochim. Biophys. Acta* **1833**, 381–387 (2013).
- Bittner, L.-M., Arends, J. & Narberhaus, F. When, how and why? Regulated proteolysis by the essential FtsH protease in *Escherichia coli*. *Biol. Chem.* **398**, 625–635 (2017).
- Fivenson, E. M. & Bernhardt, T. G. An essential membrane protein modulates the proteolysis of LpxC to control lipopolysaccharide synthesis in *Escherichia coli*. *mBio*. **11**, e00939–00920 (2016).
- van Stelten, J., Silva, F., Belin, D. & Silhavy, T. J. Effects of antibiotics and a proto-oncogene homolog on destruction of protein translocator SecY. *Science* **325**, 753–756 (2009).
- Arsène, F., Tomoyasu, T. & Bukau, B. The heat shock response of *Escherichia coli*. *Int. J. Food Microbiol.* **55**, 3–9 (2000).
- Lee, H. B., Park, S. H. & Lee, C.-R. The inner membrane protein LapB is required for adaptation to cold stress in an LpxC-independent manner. *J. Microbiol.* **59**, 666–674 (2021).
- Biernacka, D., Gorzelak, P., Klein, G. & Raina, S. Regulation of the first committed step in lipopolysaccharide biosynthesis catalyzed by LpxC requires the essential protein LapC (YejM) and HslVU protease. *Int. J. Mol. Sci.* **21**, E9088 (2020).
- Guest, R. L., Samé Guerra, D., Wissler, M., Grimm, J. & Silhavy, T. J. YejM modulates activity of the YciM/FtsH protease complex to prevent lethal accumulation of lipopolysaccharide. *mBio*. **11**, e00598–00520 (2020).
- Nguyen, D., Kelly, K., Qiu, N. & Misra, R. YejM controls LpxC levels by regulating protease activity of the FtsH/YciM complex of *Escherichia coli*. *J. Bacteriol.* **202**, e00303–e00320 (2020).
- Smakowska, E., Czarna, M. & Janska, H. Mitochondrial ATP-dependent proteases in protection against accumulation of carbonylated proteins. *Mitochondrion* <https://doi.org/10.1016/j.mito.2014.03.005> (2014).
- Tatsuta, T. & Langer, T. AAA proteases in mitochondria: diverse functions of membrane-bound proteolytic machines. *Res. Microbiol.* **160**, 711–717 (2009).
- Yoshioka, M. et al. Quality control of photosystem II: FtsH hexamers are localized near photosystem II at grana for the swift repair of damage. *J. Biol. Chem.* **285**, 41972–41981 (2010).
- Nixon, P. J., Michoux, F., Yu, J., Boehm, M. & Komenda, J. Recent advances in understanding the assembly and repair of photosystem II. *Ann. Bot.* **106**, 1–16 (2010).
- Kikuchi, S. et al. A Ycf2-FtsHi heteromeric AAA-ATPase complex is required for chloroplast protein import. *Plant Cell* **30**, 2677–2703 (2018).
- Herrmann, J. M. A force-generating machine in the plant's powerhouse: A pulling AAA-ATPase motor drives protein translocation into chloroplasts. *Plant Cell* **30**, 2646–2647 (2018).
- Bieniossek, C., Niederhauser, B. & Baumann, U. M. The crystal structure of apo-FtsH reveals domain movements necessary for substrate unfolding and translocation. *Proc. Natl Acad. Sci. USA* **106**, 21579–21584 (2009).
- Suno, R. et al. Structure of the whole cytosolic region of ATP-dependent protease FtsH. *Mol. Cell* **22**, 575–585 (2006).
- Niwa, H., Tsuchiya, D., Makyio, H., Yoshida, M. & Morikawa, K. Hexameric ring structure of the ATPase domain of the membrane-integrated metalloprotease FtsH from *Thermus thermophilus* HB8. *Structure* **10**, 1415–1423 (2002).
- Vostrukhina, M. et al. The structure of Aquifex aeolicus FtsH in the ADP-bound state reveals a C2-symmetric hexamer. *Acta Crystallogr. D. Struct. Biol.* **71**, 1307–1318 (2015).
- Bieniossek, C. et al. The molecular architecture of the metalloprotease FtsH. *Proc. Natl Acad. Sci. USA* **103**, 3066–3071 (2006).
- Puchades, C. et al. Structure of the mitochondrial inner membrane AAA+ protease YME1 gives insight into substrate processing. *Science* **358**, ea00464 (2017).
- Gates, S. N. & Martin, A. Stairway to translocation: AAA+ motor structures reveal the mechanisms of ATP-dependent substrate translocation. *Protein Sci.* **29**, 407–419 (2020).
- Lee, S. et al. Electron cryomicroscopy structure of a membrane-anchored mitochondrial AAA protease. *J. Biol. Chem.* **286**, 4404–4411 (2011).
- Jumper, J. et al. Highly accurate protein structure prediction with AlphaFold. *Nature* **596**, 583–589 (2021).
- Carvalho, V. et al. The cytoplasmic domain of the AAA+ protease FtsH is tilted with respect to the membrane to facilitate substrate entry. *J. Biol. Chem.* **296**, 100029 (2021).
- Uthoff, M. & Baumann, U. Conformational flexibility of pore loop-1 gives insights into substrate translocation by the AAA+ protease FtsH. *J. Struct. Biol.* **204**, 199–206 (2018).
- Westphal, K., Langklotz, S., Thomanek, N. & Narberhaus, F. A trapping approach reveals novel substrates and physiological functions of the essential protease FtsH in *Escherichia coli*. *J. Biol. Chem.* **287**, 42962–42971 (2012).
- Puchades, C., Sandate, C. R. & Lander, G. C. The molecular principles governing the activity and functional diversity of AAA+ proteins. *Nat. Rev. Mol. Cell Biol.* **21**, 43–58 (2020).
- Kihara, A., Akiyama, Y. & Ito, K. Different pathways for protein degradation by the FtsH/HflKC membrane-embedded protease complex: An implication from the interference by a mutant form of a new substrate protein, YccA. *J. Mol. Biol.* **279**, 175–188 (1998).
- Arends, J., Thomanek, N., Kuhlmann, K., Marcus, K. & Narberhaus, F. In vivo trapping of FtsH substrates by label-free quantitative proteomics. *Proteomics* **16**, 3161–3172 (2016).
- Began, J. et al. Rhomboid intramembrane protease YqgP licenses bacterial membrane protein quality control as adaptor of FtsH AAA protease. *EMBO J.* **39**, e102935 (2020).
- An, J. Y. et al. Structural insights into the oligomerization of FtsH periplasmic domain from *Thermotoga maritima*. *Biochem. Biophys. Res. Commun.* **495**, 1201–1207 (2018).

36. Kater, L. et al. Structure of the Bcs1 AAA-ATPase suggests an airlock-like translocation mechanism for folded proteins. *Nat. Struct. Mol. Biol.* **27**, 142–149 (2020).
37. Tang, W. K. et al. Structures of AAA protein translocase Bcs1 suggest translocation mechanism of a folded protein. *Nat. Struct. Mol. Biol.* **27**, 202–209 (2020).
38. Bruni, R. & Kloss, B. High-throughput cloning and expression of integral membrane proteins in *Escherichia coli*. *Curr. Protoc. Protein Sci.* **74**, 29.26 (2013).
39. Xia, Y., Chu, W., Qi, Q. & Xun, L. New insights into the QuikChange™ process guide the use of Phusion DNA polymerase for site-directed mutagenesis. *Nucleic Acids Res.* **43**, e12 (2015).
40. Ritchie, T. K. et al. Chapter 11—Reconstitution of membrane proteins in phospholipid bilayer nanodiscs. *Meth. Enzymol.* **464**, 211–231 (2009).
41. Zheng, S. Q. et al. MotionCor2: Anisotropic correction of beam-induced motion for improved cryo-electron microscopy. *Nat. Meth.* **14**, 331–332 (2017).
42. Zhang, K. Gctf: Real-time CTF determination and correction. *J. Struct. Biol.* **193**, 1–12 (2016).
43. McSweeney, D. M., McSweeney, S. M. & Liu, Q. A self-supervised workflow for particle picking in cryo-EM. *IUCr* **7**, 719–727 (2020).
44. Zivanov, J. et al. New tools for automated high-resolution cryo-EM structure determination in RELION-3. *eLife* **7**, e42166 (2018).
45. Punjani, A., Zhang, H. & Fleet, D. J. Non-uniform refinement: Adaptive regularization improves single-particle cryo-EM reconstruction. *Nat. Meth.* **17**, 1214–1221 (2020).
46. Pettersen, E. F. et al. UCSF chimera—A visualization system for exploratory research and analysis. *J. Comput. Chem.* **25**, 1605–1612 (2004).
47. Vilas, J. et al. Local resolution estimates of cryoEM reconstructions. *Curr. Opin. Struct. Biol.* **64**, 74–78 (2020).
48. Adams, P. D. et al. PHENIX: A comprehensive Python-based system for macromolecular structure solution. *Acta Crystallogr. D. Struct. Biol.* **66**, 213–221 (2010).
49. Casañal, A., Lohkamp, B. & Emsley, P. Current developments in Coot for macromolecular model building of electron cryo-microscopy and crystallographic data. *Protein Sci.* **29**, 1055–1064 (2020).
50. Williams, C. J. et al. MolProbity: More and better reference data for improved all-atom structure validation. *Protein Sci.* **27**, 293–315 (2018).
51. Mirdita, M. et al. ColabFold-making protein folding accessible to all. Preprint at *bioRxiv*. <https://doi.org/10.1101/2021.08.15.456425> (2021).

Acknowledgements

We thank Huilin Li for helpful discussions and suggestions, Minge Du and Zuanning Yuan for screening cryo-EM samples, LBMS staff for the help with the cryo-EM operation and data acquisition. Q.L. was supported by the U.S. Department of Energy (DOE), Office of Biological and Environmental Research as part of the Quantitative Plant

Science Initiative at Brookhaven National Laboratory. T.W. was supported in part by a PSC-CUNY Award 64507-00 52, jointly funded by the Professional Staff Congress and the City University of New York. The work used Laboratory for Biomolecular Structure (LBMS) which is supported by the U.S. Department of Energy, Office of Science, Office of Biological and Environmental Research.

Author contributions

T.W. and Q.L. designed the study and experiments. W.L., T.W., M.S., and Q.L. performed the experiments. T.W., S.M., and Q. L. analyzed the data. Q.L. wrote the manuscript with help from other coauthors.

Competing interests

The authors declare no competing interests.

Additional information

Supplementary information The online version contains supplementary material available at <https://doi.org/10.1038/s42003-022-03213-2>.

Correspondence and requests for materials should be addressed to Tong Wang or Qun Liu.

Peer review information *Communications Biology* thanks Soo Hyun Eom, Youdong Mao, and the other, anonymous, reviewers for their contribution to the peer review of this work. Primary Handling Editors: Janesh Kumar and Gene Chong. Peer reviewer reports are available.

Reprints and permission information is available at <http://www.nature.com/reprints>

Publisher's note Springer Nature remains neutral with regard to jurisdictional claims in published maps and institutional affiliations.



Open Access This article is licensed under a Creative Commons Attribution 4.0 International License, which permits use, sharing, adaptation, distribution and reproduction in any medium or format, as long as you give appropriate credit to the original author(s) and the source, provide a link to the Creative Commons license, and indicate if changes were made. The images or other third party material in this article are included in the article's Creative Commons license, unless indicated otherwise in a credit line to the material. If material is not included in the article's Creative Commons license and your intended use is not permitted by statutory regulation or exceeds the permitted use, you will need to obtain permission directly from the copyright holder. To view a copy of this license, visit <http://creativecommons.org/licenses/by/4.0/>.

© The Author(s) 2022